Dense vegetation promotes denudation in Patagonian rainforests

Christian H Mohr[1], Violeta Tolorza[2], Viktoria Georgieva[3], Henry Munack[4], Klaus M Wilcken[5], Réka-Hajnalka Fülöp[5], Alexandru T Codilean[4], Eric Parra[1] and Sebastien Carretier[6]

[1]University of Potsdam, Institute of Environmental Sciences and Geography, 14476 Potsdam, Germany, cmohr@uni-potsdam, eric.parra.hormazabal@uni-potsdam.de

[2]Universidad de la Frontera, Department of Civil Engineering, Faculty of Engineering and Sciences. 4811230 Temuco, Chile, violeta.tolorza@ufrontera.cl

[3]Universidad Austral de Chile, Institute of Physics and Mathematics, Faculty of Science, Edificio Pugín - Campus Isla Teja, Valdivia, Chile, viktoria.georgieva@uach.cl

[4]School of Earth, Atmospheric and Life Sciences, and ARC Centre of Excellence for Australian Biodiversity and Heritage, University of Wollongong, Wollongong, NSW 2522, Australia, henrymunack@gmail.com, codilean@uow.edu.au

[5]Australian Nuclear Science and Technology Organisation (ANSTO), Lucas Heights, NSW 2234, Australia, klaus.wilcken@ansto.gov.au, rekaf@ansto.gov.au

[6]Géosciences Environment Toulouse (GET), Université de Toulouse, IRD, UPS, CNRS, 31400 Toulouse, France, sebastien.carretier@get.omp.eu

Corresponding author: University of Potsdam, Institute of Environmental Sciences and Geography, 14476 Potsdam, Germany, cmohr@uni-potsdam

A geomorphological key paradigm predicts that intact forests are erosional idle, however comprise an efficient weathering machine sustaining high soil production rates. Only during times of disturbance, e.g., by earthquakes, those forests are observed to jump up to high-erosion-state, then being capable of releasing some of Earth's highest sediment yields involving massive pulses of organic carbon. Coastal temperate rainforests, in particular, do not only store unparalleled carbon stocks building up a globally important carbon sink, but are also home to high (endemic) biodiversity. Here we document extraordinarily high catchment-averaged denudation rates, across multiple disturbance cycles, under the dense vegetation of the Patagonian rainforests. There, ^{10}Be-derived denudation rates of >0.8 m kyr^{-1} exceed any known value from the entire Chilean Andes orogen, a highly variable >3.000 km long natural laboratory involving steep climatic and topographic gradients. We argue that such high denudation rates are consistent with a first-order control of the rainforest itself. High biomass loads exert a soil surcharge that promotes landsliding already along a relatively low critical slope angle. In contrast, denudation rates from more arid, and less forested sectors of the Chilean Andes – though going along with steeper critical slope angles – remain below half of our new rates derived from the Patagonian rainforests. Taken together, our study provides indication that denudation, to a higher degree than hitherto agreed on, operates as a continuous process involving soil production, vegetation, physical erosion and ecohydrological processes. Such a holistic denudational continuum, finally, is different from prevailing views that vegetation generally stabilizes hillslopes, thus promoting steep slope gradients, however, limiting landsliding activity.

Keywords: Patagonia; Coastal Temperate Rainforest; Denudation; ^{10}Be; Chile

Forests, disturbances, and denudation

Aside from regulating climate patterns [1] and accumulating carbon from the atmosphere to build up important global carbon sinks[2], intact forests are essential to Earth's habitats because they protect soils from erosion[3]. In turn, forest disturbance, such as deforestation, wildfires, earthquakes, or windstorms promote erosion[e.g., 4,5] by exposing bare surfaces to erosive rainfall, reducing evapotranspiration, or weakening slope and river-bank stability through reduced soil cohesion and root anchoring[3]. Yet, some of Earth's highest denudation rates, i.e., the mass removal from Earth's surface by combined erosion and weathering processes, have been derived from lush coastal temperate rainforests, for instance those covering the New Zealand's Southern Alps[e.g., 4]. There, steep slopes frequently fail despite sustaining dense, pristine forests gathering system-relevant amounts of carbon[5,6], thus conditioning young landscape ages with respectively short forest turnover times of these ecosystems[e.g., 5]. High precipitation rates required to sustain dense vegetation enhance denudation, potentially exceeding vegetation's anchoring effects[7]. Under undisturbed conditions, however, such rainfall-denudation scaling is non-monotonic[8–10] and denudation rates break down after vegetation cover exceeds 50-85%[7]. Yet, quantifying disturbances' long-term contribution to total denudation remains poorly documented because of the annual or at most decadal focus of disturbance-related erosion studies, with a few noticeable exceptions[e.g., 11]. However, such information is not only needed to estimate the effect of single disturbances on geomorphic processes[e.g., 11], but also to assess the functioning of forests as carbon sources or sinks over hundreds to thousands of years. Leaning on the cyclic concepts of disturbance ecology[12], we define long-term here as the timespan that covers multiple disturbance cycles typical to the regional disturbance regime, allowing an eco-geomorphic system to recover to a pre-disturbance state. As will be shown in the following, ubiquitous in situ ^{10}Be is a particularly

suitable nuclide for denudation studies on such time scales[13,14] for two reasons: First, it does not integrate too long back into the past, hence justifying the strong assumption of stable vegetation cover throughout the period constrained by the data. Second, despite the latter, ^{10}Be's averaging timescale still embraces multiple disturbance cycles.

The Coastal Rainforests of Patagonia

The coastal temperate rainforests (abbreviated as CTR) of Northern Patagonia form part of the Valdivian Rainforest Biome, a global ecological hotspot[15] ranking among the most organic carbon rich biomes on Earth[16]. The CTRs of Northern Patagonia are marked by a cool Pacific maritime, continuously wet climate (2,000 – 4,500 mm precipitation yr^{-1})[17]. This climate promotes dense, contiguous evergreen broadleaf forests[17,18] that mostly consist of *Nothofagus nitida*, *Podocarpus nubigenus*, *Drimys winterii*, *Amomyrtus meli* and *Luma apiculata*[6,19]. Following an abrupt expansion of the forest cover at around 17,800 BP[20], these forests generally remained unchanged in composition and spatial extent at least during the last 1,000-2,000 years[21]. Early human occupation was intermittent and thus unlikely disturbing forests. First noticeable human-made disturbances followed the arrival of European and Chilean settlers in the late 19th century[22,23] who settled mostly in the lowland given inaccessibility of higher valleys. Furthermore, insect or pest-driven mortality is much less important than in drier forests[24]. Relevant fire has been absent for >11,000 years[24,25]. Instead, landslides are the prime, though consequential disturbance agent[e.g., 26,27]. Recent disturbances by earthquakes[28], volcanic eruptions[29], or winds[30] enabled hundreds of landslides on hillslopes formerly sustaining dense forest vegetation. Estimated recurrence intervals for important earthquakes and volcanic eruptions (>M8 and VEI 4, respectively) are around 10^2 years, respectively[6,31]. Severe

windstorms occur on the yearly to decadal scale[e.g., 32]. Given said regional disturbance regime, we regard ^{10}Be as an excellent candidate as it integrates over a long enough timescale to cover multiple disturbance cycles and so is suitable for looking at the effect of 'ecological' disturbance on denudation and erosion.

Denudation of Coastal Temperate Rainforests

Here we present first ^{10}Be denudation rate estimates for the Patagonian CTR (Figure 1). We contextualize those rates using a compilation of published, recalculated catchment-wide ^{10}Be denudation rates along the Chilean Andes. With slope gradients between 50 and 70%, our study catchments are relatively steep. They are underlain mostly by granitoid lithologies[33] covered by soils thinner than 2m[29] (see also Supplementary Figure 2C), which in turn set a maximum bound for shallow landslide thickness. Deeper-seated landslides involving bedrock are rare exceptions[e.g., 26,27]. Our catchments under investigation are comparable in size, i.e., 4-28 km^2 and do merely extend into the highest elevated parts of the Andes Cordillera, thus leaving only a small part of the catchments above the treeline. Despite the overall low elevation of this Andes sector, several peaks exceed well above 2,500 m asl. Mean annual precipitation (MAP) and mean annual potential evapotranspiration (MEP) is 1,600-2,700 mm and 630-810 mm, respectively, yielding aridity indices (AI) – i.e., the ratio between MAP and MEP[34] – well above 1.66. From here on, we distinguish between humid ($AI > 1$) and arid ($AI < 1$) conditions, respectively[34]. The high evapotranspiration rates are mainly due to the dense forest vegetation that covers large parts of all studied catchments.

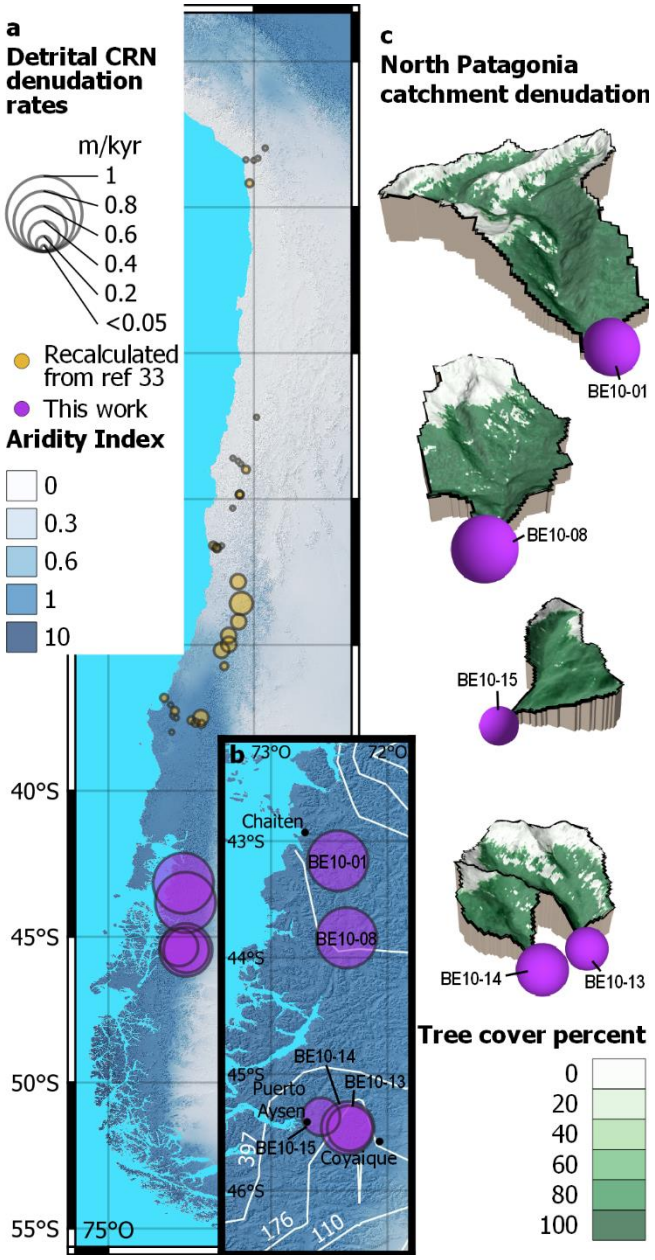

Figure 1. Catchment-averaged CRN denudation rates across the Western Chilean Andes orogen. (a) Denudation rates in m kyr^{-1}, estimated by detrital ^{10}Be using grain size range 0.125-1.00 mm compiled by Ref [35] (yellow) and this study (purple) for the north Patagonian CTR overlaying the Aridity Index (AI). (b) Study area, denudation rates, and iso-lines of annual groundwater recharge in mm yr^{-1} Ref36. (c) 2.5D-representations of studied catchments with respective denudation rates (m kyr^{-1}) and tree cover (%)[37]. Bubble size scaling applies to all figures. Numbers refer to sample IDs (see Supplementary Table 2).

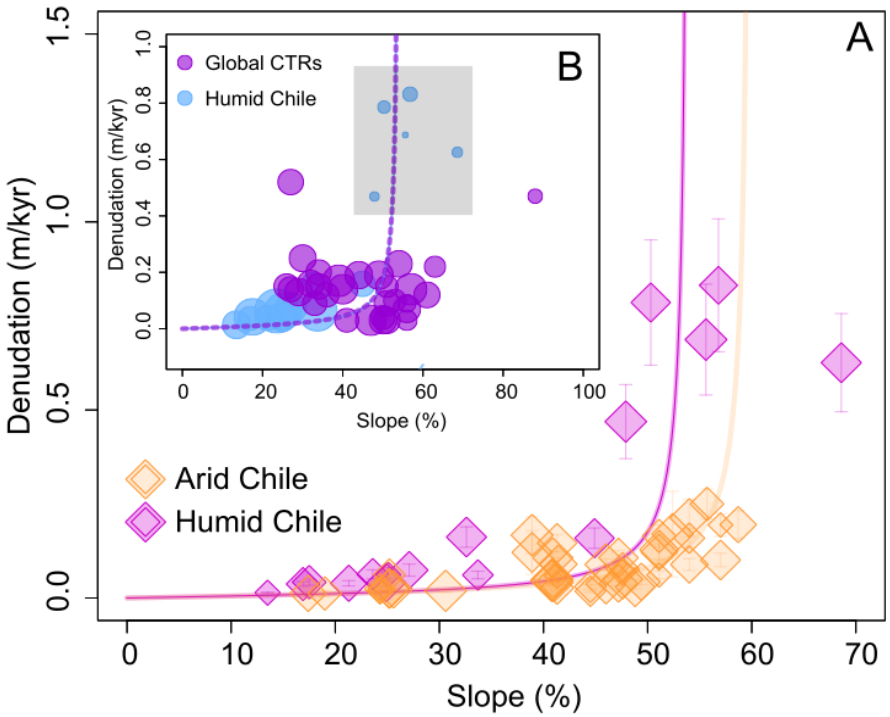

Figure 2. Denudation rate vs slope. A: For humid (purple) and arid (orange) conditions along the Chilean Andes Orogen. Purple and orange lines are models[41] considering 54% and 60% for critical slopes. Error bars refer to ± 1σ. B: Denudation rate vs slope. The violet circles refer to compiled ^{10}Be denudation rates from the OCTOPUS database[35] from New Zealand[38,39] and the Pacific Northwest[40]. The blue circles refer to humid Chile[42–44] and our new data, that is highlighted by the grey frame. Circle size scales with $\log_{10}$ of catchment size, and purple dashed line is the refers to the purple model in A [41].

With up to 0.83 m kyr^{-1} (Supplementary Table 2), our new denudation rate estimates exceed any previously published rates from fluvial sands in Chile (Figure 2A, 3A). Our new denudation rates rival the maximum rates (>85-quantile) from formerly glaciated, largely forest covered landscapes with similar climate, such as New Zealand[38,39], and the Pacific Northwest[40] (Figure 2B). Together with the Patagonian rainforest, these regions form the bulk of the global CTR Biome. Denudation rates are often reported to positively scale with precipitation under diverse climatic regimes[e.g., 45], but to be in negative relationship to vegetation cover[8–10]. Our high

rates, however, coincide with both the highest fractions of forest cover and highest humidity along the Chilean Andean orogen (Figure3A) where forest cover mimics MAP (R^2=0.77). The same general pattern holds true for MAP, yet with lower predictive power, i.e., R^2=0.52 (Supplementary Figure 1). For humid conditions, AI predicts denudation rates much better than precipitation (R^2 =0.84) (Figure 3B). In this context, we recall that unlike precipitation, AI recognizes evapotranspiration, and thus includes the biotic processes of root water uptake and interception. In contrast, abiotic precipitation did not perform as a suitable predictor (Figure 4). Consequently, we suggest AI's explanatory power for catchment-averaged denudation rates to represent a positive relationship between forest cover and denudation. With 1,600-2,700 mm annual precipitation[46] and annual groundwater recharge of 180-400 mm[36] (Figure 1B), evapotranspiration in native forests (630-810 mm yr^{-1})[47] forms an integral part of the regional water balance, equaling 25-50% of the precipitation amount. Simplifying for hydrological years, i.e., assuming zero interannual net changes in soil water[e.g., 49], the amount of evapotranspiration loss is relevant for the regional hydrology. Diurnal streamflow oscillations may reflect such losses in the absence of 'noise', e.g., rainfall[48]. In fact, we see such diurnal cycles in catchments across the Valdivian rainforest biome. AI accounts for evapotranspiration effect of the forest cover on the regional hydrology which, in turn, is neglected by abiotic precipitation. Consequently, our findings suggest that ecohydrological processes, such as evapotranspiration, need to be accounted for when comparing denudation rates on centennial to millennial time scales across biomes.

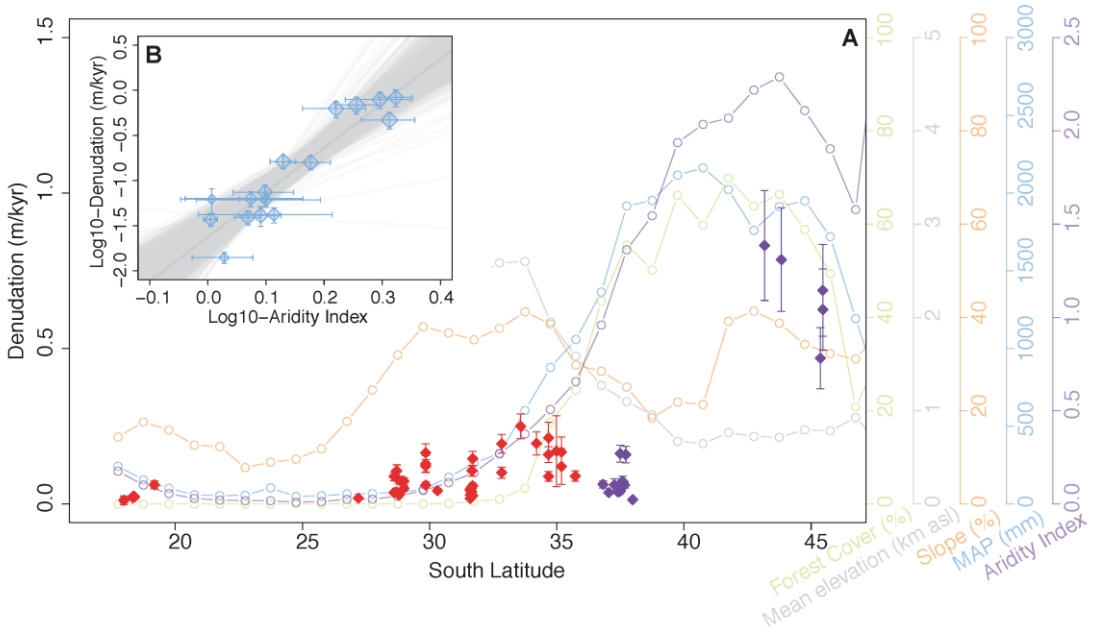

Figure 3. A: Denudation rates, forest cover, mean elevation, slope, mean annual precipitation (MAP), and aridity index (AI) along a N-S transect of the Chilean Main Cordillera. Red and violet squares refer to arid and humid climate, respectively. B: Scaling between denudation rates and the aridity index for humid climate, i.e., AI >1 (R^2 =0.84, 10,000 Monte-Carlo simulations, y=-1.625±0.10 * 4.925±0.55^x), squares scale with NDVI (Normalized Difference Vegetation Index).

With 0.63 m kyr^{-1}, the catchment with highest average elevation (BE-13), is not among the fastest denuding catchments of our dataset. From this observation we infer that it is not freeze-thaw related processes, e.g., frost driven bedrock erosion[49], that is mainly recorded in our ^{10}Be data. Instead, frequent shallow landsliding is the key erosive [27,29,30] process in the Patagonian CTRs providing sediment to the drainage network (Supplementary Figure 2c). Hence, we conclude that supply is not limiting denudation in these forests. Instead, transport-limited fluvial erosion controls sediment export.

Given the rather shallow soil depths, the idea of biotic controls on denudation on centennial to millennial time scales is congruent with a lower ‘humid’ critical slope angle, i.e., 54 %,

173 compared to arid conditions (60 % (Figure 2A). Ref[50] report denudation rates increasing
174 nonlinearly with slope for the Chilean Andean Orogen. However, a lower 'humid' critical slope
175 angle suggests, that in the presence of vegetation, catchments are more prone to denudation for a
176 given slope gradient. This may seem counter-intuitive at first sight, because vegetation is
177 commonly considered to stabilize hillslopes by root anchoring[e.g., 51]. How can dense vegetation
178 cause enhanced denudation?

179 With up to 1,000 Mg ha^{-1} [e.g., 6,47] of biomass, Patagonian CTRs are among Earth's 'heaviest'
180 biomes[16]. For a given slope gradient, such high biomass loads may be sufficient to cause failure
181 of hillslopes that would have been otherwise stable, simply driven by their own weight[52]. Cyclic
182 biomass surcharge following disturbances may lead to a tipping-bucket response to landsliding
183 largely confined into steep hilltops[53]. Our results support the notion of hillslope failures generally
184 being constrained to steep slopes (Fig. 4). Averaged over the last 20 years without obvious
185 disturbance impairment[27,29,30], landslide erosion has lowered the landscape by ~ 0.4 m kyr^{-1} (see
186 data for Huequi in Supplementary Table 3). These erosion rates are too low to exclusively explain
187 the high denudation rates within the Patagonian CTRs. From a denudational perspective, these
188 forests are apparently capable of efficiently adding to, though with the help of, mass wasting
189 effects. Weathering may benefit from vegetation as well[7]. We cannot quantify weathering rates
190 due to the lack of suitable data. However, judging from sites with comparably productive forests
191 under similar humid climates[55], we anticipate soil production rates of ≤ 0.5 mm yr^{-1} for the
192 Patagonian CTRs. As we can then assume that rates of both erosion and soil production are largely
193 equivalent, we therefore regard the study area as largely in quasi steady state. When summing up
194 both rates, we come close to our observed denudation rates. Hence, our findings imply that
195 denudation operates as a more continuous process involving soil production, vegetation, and

physical erosion. Such a holistic denudational continuum, finally, is different from prevailing views that vegetation stabilizes hillslopes, leading to steep slopes with relatively little landsliding[e.g., 54]. The higher rates we report here slightly exceed previously published exhumation rates derived from low-temperature thermochronology and constraining the record of Patagonian glaciations (5-7 Myr) along the Patagonian Andes yielding 0.2-0.7 m kyr^{-1} [Ref56–58]. Thermochronology derived rates average a period, of which we can assume at most the last 16,000 years as comparable to the current forest conditions[e.g., 20]. Given the promoting effect of the forests on denudation, however, we might be looking at higher post-glacial compared to glacial denudation rates. Consistently, we may therefore treat our results to be a realistic representation of post-glacial denudation within the Patagonian CTRs but rule out depletion effects in ^{10}Be due to a glacial heritage.

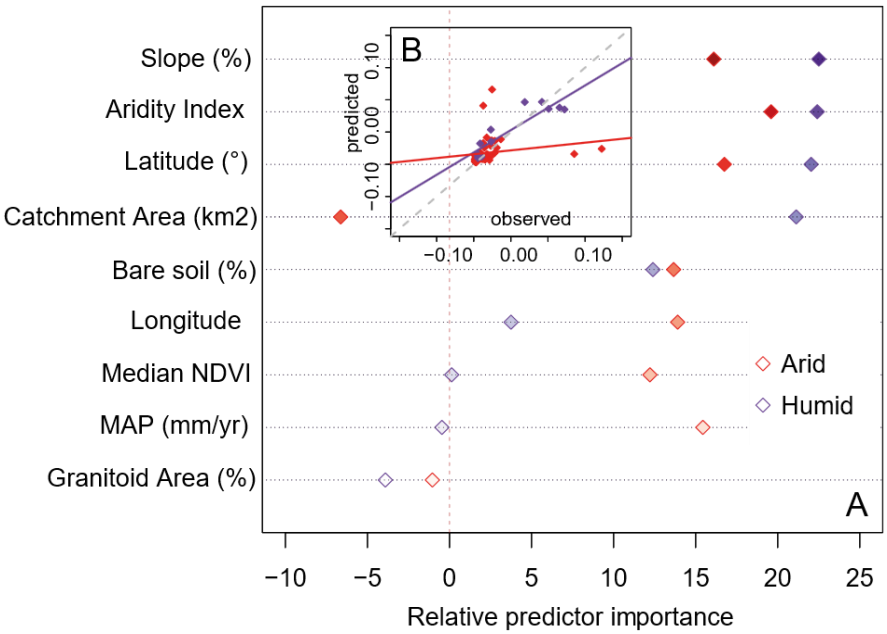

Figure 4. A: Relative variable importance for humid (*n*=12) and arid (*n*=50) conditions, respectively, for the random forest regression of ^{10}Be denudation rates from Chile (see SI). All predictor variable importance was normalized to 100% (see SI), color density scales with relative importance. B:

Observed vs predicted values for standardized denudation rates for humid (purple) and arid (red) conditions, respectively. Purple and red lines refer to linear regressions; grey dashed line refers to the 1:1-line. We treat latitude, however, as a metric that integrates large scale climatic and environmental conditions, thus largely mimicking AI.

The last glaciation in the study area ceased around 17,500 BP, followed by an extensive Andean deglaciation within just 1,000 years[20] and the fast succession of evergreen temperate rainforests. Our study catchments do not extent into unvegetated high-Andean regions but sustain a dense and continuous forest cover (Figure 1, Supplementary Table 1). Furthermore, we could not identify any glacial heritage, such as moraine deposits, or striations. In fact, abundant boulders and large grain sizes of fluvial deposits support the notion of active recent erosion within the active channels of local rivers rather than reworking of glacial sediment (Supplementary Figure 2a). Hence, we regard the reworking of glacial deposits as negligible, and thus consider depletion effects in ^{10}Be implausible. Our own modeling exercise to test for a possible glacial erosion inheritance (Supplementary Figure 3) underpins that cosmogenic detrital ^{10}Be records post-glacial conditions in mountainous regions that were glaciated in the past.

Over timespans of less than 400 years, forest may stop accumulating carbon[59], though carbon accumulation progressively scales with time since forest disturbance at the scale of individual trees[60]. These two opposing trends condition our understanding for how forest disturbances may distribute broad-scale carbon stocks within each single pool of the carbon cycle. An active disturbance regime promotes carbon export on time scales that may comprise multiple disturbance events[61]. Given the minimal impact of human activity across the Patagonian rainforests, a primary production rate of around 600 gC m^{-2} yr^{-1} Ref6 and denudation rates averaged over 720-1,300 years, our study provides a benchmark to assess modern denudation and landscape turnover rates against

presumably undisturbed forest conditions in one of the global hotspots for biodiversity and organic carbon[62].

ACKNOWLEDGMENTS

CHM acknowledges funding provided by DFG grant # 493703771. VT received funding by postdoc grant VRIP20P001 and FONDECYT 11190864 supporting this research. EP received funding from Agencia Nacional de Investigación y Desarrollo, Chile (ANID) and the German Academic Exchange Service, Germany (DAAD). HM benefited from an Endeavour Research Fellowship (#5547-2016) granted by the Australian Government. VG received funding by an ANID/FONDECYT Postdoctoral Grant 2020 °N3200375. Drone footage for SI figure 5 was acquired and provided by Benjamin Sotomayor. The authors acknowledge support from the Center for Accelerator Science at Australian Nuclear Science and Technology Organisation (ANSTO) through the National Collaborative Research Infrastructure Strategy (NCRIS).

REFERENCES CITED

1. Bonan, G. B. Forests and Climate Change: Forcings, Feedbacks, and the Climate Benefits of Forests. *Science (1979)* **320**, 1444–1449 (2008).
2. Canadell, J. G. & Raupach, M. R. Managing forests for climate change mitigation. *Science (1979)* **320**, 1456–1457 (2008).
3. Sidle, R. C. & Ochiai, H. Land Use and Global Change. in *Landslides: Processes, Prediction, and Land Use* 1–76 (2006).
4. Korup, O., McSaveney, M. J. & Davies, T. R. H. Sediment generation and delivery from large historic landslides in the Southern Alps, New Zealand. *Geomorphology* **61**, 189–207 (2004).
5. Hilton, R. G., Meunier, P., Hovius, N., Bellingham, P. J. & Galy, A. Landslide impact on organic carbon cycling in a temperate montane forest. *Earth Surface Processes and Landforms* **36**, 1670–1679 (2011).
6. Mohr, C. H., Korup, O., Ulloa, H. & Iroumé, A. Pyroclastic Eruption Boosts Organic Carbon Fluxes Into Patagonian Fjords. *Global Biogeochemical Cycles* **31**, 1626–1638 (2017).

7. Starke, J., Ehlers, T. A. & Schaller, M. Latitudinal effect of vegetation on erosion rates identified along western South America. *Science (1979)* **367**, 1358–1361 (2020).
8. Langbein, W. B. & Schumm, S. A. Yield of sediment in relation to mean annual precipitation. *Transactions, American Geophysical Union* **39**, 1076 (1958).
9. Acosta, V. T. *et al.* Effect of vegetation cover on millennial-scale landscape denudation rates in East Africa. *Lithosphere* **7**, 408–420 (2015).
10. Schmid, M., Ehlers, T. A., Werner, C., Hickler, T. & Fuentes-Espoz, J. P. Effect of changing vegetation and precipitation on denudation - Part 2: Predicted landscape response to transient climate and vegetation cover over millennial to million-year timescales. *Earth Surface Dynamics* **6**, 859–881 (2018).
11. Vanacker, V. *et al.* Restoring dense vegetation can slow mountain erosion to near natural benchmark levels. *Geology* **35**, 303 (2007).
12. Turner, M. G., Romme, W. H., Gardner, R. H., O'neill, R. v & Kratz, T. K. *A revised concept of landscape equilibrium: Disturbance and stability on scaled landscapes*. *Landscape Ecology* vol. 8 (1993).
13. Granger, D. E. & Schaller, M. Cosmogenic Nuclides and Erosion at the Watershed Scale. *Elements* **10**, 369–373 (2014).
14. Schaefer, J. M. *et al.* Cosmogenic nuclide techniques. *Nature Reviews Methods Primers* **2**, 18 (2022).
15. Myers, N., Mittermeier, R. A., Mittermeier, C. G., da Fonseca, G. A. B. & Kent, J. Biodiversity hotspots for conservation priorities. *Nature* **403**, 853–858 (2000).
16. Keith, H., Mackey, B. G. & Lindenmayer, D. B. Re-evaluation of forest biomass carbon stocks and lessons from the world's most carbon-dense forests. *Proc Natl Acad Sci U S A* **106**, 11635–11640 (2009).
17. DellaSala, D. A. *Temperate and Boreal Rainforests of the World: Ecology and Conservation*. (Island Press/Center for Resource Economics, 2011). doi:10.5822/978-1-61091-008-8.
18. Alaback, P. Comparative ecology of temperate rainforests of the Americas along analogous climatic gradients. *Revista Chilena de Historia Natural* **64**, 399–412 (1991).
19. de La Barrera, F., Reyes-Paecke, S. & Meza, L. Landscape analysis for rapid ecological assessment of relocation alternatives for a devastated city. *Revista Chilena de Historia Natural* **84**, 181–194 (2011).
20. Moreno, P. I. *et al.* Radiocarbon chronology of the last glacial maximum and its termination in northwestern Patagonia. *Quaternary Science Reviews* **122**, 233–249 (2015).
21. de Porras, M. E. *et al.* Postglacial vegetation, fire and climate dynamics at Central Chilean Patagonia (Lake Shaman, 44°S). *Quaternary Science Reviews* **50**, 71–85 (2012).
22. Torrejón, F., Cisternas, M., Alvial, I. & Torres, L. Colonial timber felling consequences of the alerce forests in Chiloé, southern Chile (18th and 19th centuries). *Magallania (Punta Arenas)* **39**, 75–95 (2011).
23. Urbina, M. X. Análisis histórico-cultural del alerce en la Patagonia septentrional occidental, Chiloé, siglos XVI al XIX. *Magallania (Punta Arenas)* **39**, 57–73 (2011).
24. Buma, B. *et al.* Emergent freeze and fire disturbance dynamics in temperate rainforests. *Austral Ecology* **44**, 812–826 (2019).
25. Markgraf, V. & Huber, U. M. Late and postglacial vegetation and fire history in Southern Patagonia and Tierra del Fuego. *Palaeogeography, Palaeoclimatology, Palaeoecology* **297**, 351–366 (2010).

26. Sommerfeld, A. *et al.* Patterns and drivers of recent disturbances across the temperate forest biome. *Nature Communications* **9**, (2018).
27. Morales, B. *et al.* A comparative machine learning approach to identify landslide triggering factors in northern Chilean Patagonia. *Landslides* **18**, 2767–2784 (2021).
28. Sepúlveda, S. A., Serey, A., Lara, M., Pavez, A. & Rebolledo, S. Landslides induced by the April 2007 Aysén fjord earthquake, Chilean Patagonia. *Landslides* **7**, 483–492 (2010).
29. Korup, O., Seidemann, J. & Mohr, C. H. Increased landslide activity on forested hillslopes following two recent volcanic eruptions in Chile. *Nature Geoscience* 2–8 (2019) doi:10.1038/s41561-019-0315-9.
30. Parra, E., Mohr, C. & Korup, O. Predicting Patagonian Landslides: Roles of Forest Cover and Wind Speed. (2021) doi:10.1029/2021GL095224.
31. Mohr, C. H., Manga, M., Wang, C. Y. & Korup, O. Regional changes in streamflow after a megathrust earthquake. *Earth and Planetary Science Letters* **458**, 418–428 (2017).
32. Veblen, T. Forest development in tree-fall gaps in the temperate rain forest of Chile. *Natl. Geogr. Res.* **1**, 162–183 (1985).
33. Sernageomin. Mapa geologico de chile: version digital. *Publicacion Geologia Digital* vol. 4 25 (2003).
34. Zomer, R. J. *et al. Trees and Water: Smallholder Agroforestry on Irrigated Lands in Northern India*. *IWMI report* (2007).
35. Codilean, A. T. *et al.* OCTOPUS: an open cosmogenic isotope and luminescence database. *Earth System Science Data* **10**, 2123–2139 (2018).
36. Müller Schmied, H. *et al.* Sensitivity of simulated global-scale freshwater fluxes and storages to input data, hydrological model structure, human water use and calibration. *Hydrology and Earth System Sciences* **18**, 3511–3538 (2014).
37. Hansen, M. C. *et al.* High-Resolution Global Maps of 21st-Century Forest Cover Change. *Science (1979)* **342**, 850–853 (2013).
38. Burdis, A. J. Denudation rates derived from spatially-averaged cosmogenic nuclide analysis in Nelson/Tasman catchments, South Island, New Zealand. (Victoria University of Wellington, 2014).
39. Bellingham, M. F. Climatic effects on rapid chemical and physical denudation rates measured with cosmogenic nuclides in the Ōhau catchment, New Zealand. (Victoria University of Wellington, 2020).
40. Moon, S. *et al.* Climatic control of denudation in the deglaciated landscape of the Washington Cascades. *Nature Geoscience* **4**, 469–473 (2011).
41. Roering, J. J., Perron, J. T. & Kirchner, J. W. Functional relationships between denudation and hillslope form and relief. *Earth and Planetary Science Letters* **264**, 245–258 (2007).
42. Carretier, S. *et al.* Erosion in the Chilean Andes between 27°S and 39°S: tectonic, climatic and geomorphic control. *Geological Society, London, Special Publications* **399**, 401–418 (2015).
43. Carretier, S. *et al.* Differences in 10Be concentrations between river sand, gravel and pebbles along the western side of the central Andes. *Quaternary Geochronology* **27**, 33–51 (2015).
44. Tolorza, V. Magnitude and Dynamics of catchment erosion in the Biobío River Basin. (Universidad de Chile, 2015).
45. Mishra, A. K., Placzek, C. & Jones, R. Coupled influence of precipitation and vegetation on millennial-scale erosion rates derived from 10Be. *PLOS ONE* **14**, e0211325 (2019).

46. Alvarez-Garreton, C. *et al.* The CAMELS-CL dataset: catchment attributes and meteorology for large sample studies – Chile dataset. *Hydrology and Earth System Sciences Discussions* 1–40 (2018) doi:10.5194/hess-2018-23.
47. Urrutia-Jalabert, R., Malhi, Y. & Lara, A. The Oldest, Slowest Rainforests in the World? Massive Biomass and Slow Carbon Dynamics of Fitzroya cupressoides Temperate Forests in Southern Chile. *PLOS ONE* **10**, e0137569 (2015).
48. Mohr, C. H., Manga, M., Wang, C., Kirchner, J. W. & Bronstert, A. Shaking water out of soil. *Geology* **43**, 207–210 (2015).
49. Hales, T. C. & Roering, J. J. Climatic controls on frost cracking and implications for the evolution of bedrock landscapes. *Journal of Geophysical Research* **112**, F02033 (2007).
50. Carretier, S. *et al.* Slope and climate variability control of erosion in the Andes of central Chile. *Geology* **41**, 195–198 (2013).
51. Sidle, R. C. A Conceptual Model of Changes in Root Cohesion in Response to Vegetation Management. *Journal of Environmental Quality* **20**, 43–52 (1991).
52. Vorpahl, P., Dislich, C., Elsenbeer, H., Märker, M. & Schröder, B. Biotic controls on shallow translational landslides. *Earth Surface Processes and Landforms* **38**, 198–212 (2013).
53. Spors, S. Suicidal forests ? – Modelling biomass surcharge as a potential landslide driver in temperate rainforests of Chilean Patagonia. (Universität Potsdam, 2021).
54. Larsen, I. J., Montgomery, D. R. & Korup, O. Landslide erosion controlled by hillslope material. *Nature Geoscience* **3**, 247–251 (2010).
55. Amundson, R., Heimsath, A., Owen, J., Yoo, K. & Dietrich, W. E. Hillslope soils and vegetation. *Geomorphology* **234**, 122–132 (2015).
56. Fosdick, J. C., Grove, M., Hourigan, J. K. & Calderón, M. Retroarc deformation and exhumation near the end of the Andes, southern Patagonia. *Earth and Planetary Science Letters* **361**, 504–517 (2013).
57. Andrić-Tomašević, N. *et al.* Quantifying Tectonic and Glacial Controls on Topography in the Patagonian Andes (46.5°S) From Integrated Thermochronometry and Thermo-Kinematic Modeling. *Journal of Geophysical Research: Earth Surface* **126**, (2021).
58. Georgieva, V. *et al.* Tectonic control on rock uplift, exhumation, and topography above an oceanic ridge collision: Southern Patagonian Andes (47°S), Chile. *Tectonics* **35**, 1317–1341 (2016).
59. Gray, A. N., Whittier, T. R. & Harmon, M. E. Carbon stocks and accumulation rates in Pacific Northwest forests: Role of stand age, plant community, and productivity. *Ecosphere* **7**, 1–19 (2016).
60. Stephenson, N. L. *et al.* Rate of tree carbon accumulation increases continuously with tree size. *Nature* **507**, 90–93 (2014).
61. Frith, N. v. *et al.* Carbon export from mountain forests enhanced by earthquake-triggered landslides over millennia. *Nature Geoscience* **11**, 772–776 (2018).
62. Smith, R. W., Bianchi, T. S., Allison, M., Savage, C. & Galy, V. High rates of organic carbon burial in fjord sediments globally. *Nature Geoscience* **8**, 450–453 (2015).
63. Singer, B. S., Ackert, R. P. & Guillou, H. 40Ar/39Ar and K-Ar chronology of Pleistocene glaciations in Patagonia. *Geological Society of America Bulletin* **116**, 434 (2004).
64. Cembrano, J., Hervé, F. & Lavenu, A. The Liquiñe Ofqui fault zone: a long-lived intra-arc fault system in southern Chile. *Tectonophysics* **259**, 55–66 (1996).

65. Pepin, E., Carretier, S., Guyot, J. L. & Escobar, F. Specific suspended sediment yields of the Andean rivers of Chile and their relationship to climate, slope and vegetation. *Hydrological Sciences Journal* **55**, 1190–1205 (2010).
66. Carretier, S. *et al.* Review of erosion dynamics along the major N-S climatic gradient in Chile and perspectives. *Geomorphology* **300**, 45–68 (2018).
67. Lal, D. Cosmic ray labeling of erosion surfaces: in situ nuclide production rates and erosion models. *Earth and Planetary Science Letters* **104**, 424–439 (1991).
68. von Blanckenburg, F. & Willenbring, J. K. Cosmogenic Nuclides: Dates and Rates of Earth-Surface Change. *Elements* **10**, 341–346 (2014).
69. Kohl, C. P. & Nishiizumi, K. Chemical isolation of quartz for measurement of in-situ -produced cosmogenic nuclides. *Geochimica et Cosmochimica Acta* **56**, 3583–3587 (1992).
70. von Blanckenburg, F., Belshaw, N. S. & O'Nions, R. K. Separation of 9Be and cosmogenic 10Be from environmental materials and SIMS isotope dilution analysis. *Chemical Geology* **129**, 93–99 (1996).
71. Wilcken, K. M. *et al.* SIRIUS Performance: 10Be, 26Al and 36Cl measurements at ANSTO. *Nuclear Instruments and Methods in Physics Research Section B: Beam Interactions with Materials and Atoms* **455**, 300–304 (2019).
72. Nishiizumi, K. *et al.* Absolute calibration of 10Be AMS standards. *Nuclear Instruments and Methods in Physics Research, Section B: Beam Interactions with Materials and Atoms* **258**, 403–413 (2007).
73. Mudd, S. M., Harel, M.-A., Hurst, M. D., Grieve, S. W. D. & Marrero, S. M. The CAIRN method: automated, reproducible calculation of catchment-averaged denudation rates from cosmogenic nuclide concentrations. *Earth Surface Dynamics* **4**, 655–674 (2016).
74. Braucher, R., Merchel, S., Borgomano, J. & Bourlès, D. L. Production of cosmogenic radionuclides at great depth: A multi element approach. *Earth and Planetary Science Letters* **309**, 1–9 (2011).
75. Jarvis, A., Reuter, H. I., Nelson, A. & Guevara, E. Hole-filled SRTM for the globe Version 4. *available from the CGIAR-CSI SRTM 90m Database* vol. 15 http://srtm.csi.cgiar.org (2008).
76. Stone, J. O. Air pressure and cosmogenic isotope production. *Journal of Geophysical Research: Solid Earth* **105**, 23753–23759 (2000).
77. Compo, G. P. *et al.* The Twentieth Century Reanalysis Project. *Quarterly Journal of the Royal Meteorological Society* vol. 137 1–28 (2011).
78. Codilean, A. T. Calculation of the cosmogenic nuclide production topographic shielding scaling factor for large areas using DEMs. *Earth Surface Processes and Landforms* **31**, 785–794 (2006).
79. Zambrano-Bigiarini, M., Nauditt, A., Birkel, C., Verbist, K. & Ribbe, L. Temporal and spatial evaluation of satellite-based rainfall estimates across the complex topographical and climatic gradients of Chile. *Hydrology and Earth System Sciences* **21**, 1295–1320 (2017).
80. Zhao, Y. *et al.* Detailed dynamic land cover mapping of Chile: Accuracy improvement by integrating multi-temporal data. *Remote Sensing of Environment* **183**, 170–185 (2016).
81. Zomer, R. J., Trabucco, A., Bossio, D. A. & Verchot, L. v. Climate change mitigation: A spatial analysis of global land suitability for clean development mechanism afforestation and reforestation. *Agriculture, Ecosystems and Environment* **126**, 67–80 (2008).

82. Gorelick, N. *et al.* Google Earth Engine: Planetary-scale geospatial analysis for everyone. *Remote Sensing of Environment* **202**, 18–27 (2017).
83. Breiman, L. Random Forests. *Machine Learning* **45**, 5–32 (2001).
84. Liaw, A. & Wiener, M. Classification and Regression by randomForest. *R News* **2**, 18–22 (2002).
85. Strobl, C., Boulesteix, A. L., Kneib, T., Augustin, T. & Zeileis, A. Conditional variable importance for random forests. *BMC Bioinformatics* **9**, 1–11 (2008).
86. Larsen, I. J. *et al.* Rapid soil production and weathering in the Southern Alps, New Zealand. *Science* **343**, 637–40 (2014).
87. Carretier, S. *et al.* A note on 10 Be-derived mean erosion rates in catchments with heterogeneous lithology: examples from the western Central Andes. *Earth Surface Processes and Landforms* **40**, 1719–1729 (2015).
88. Kober, F. *et al.* Complex multiple cosmogenic nuclide concentration and histories in the arid Rio Lluta catchment, northern Chile. *Earth Surface Processes and Landforms* **34**, 398–412 (2009).
89. Braucher, R. *et al.* Determination of muon attenuation lengths in depth profiles from in situ produced cosmogenic nuclides. *Nuclear Instruments and Methods in Physics Research Section B: Beam Interactions with Materials and Atoms* **294**, 484–490 (2013).

FIGURE CAPTIONS

Figure 5. Catchment-averaged CRN denudation rates across the Western Chilean Andes orogen. (a) Denudation rates in m kyr^{-1}, estimated by detrital ^{10}Be using grain size range 0.125-1.00 mm compiled by Ref [35] (yellow) and this study (purple) for the north Patagonian CTR overlaying the Aridity Index (AI). (b) Study area, denudation rates, and iso-lines of annual groundwater recharge in mm yr^{-1} Ref36. (c) 2.5D-representations of studied catchments with respective denudation rates (m kyr^{-1}) and tree cover (%)[37]. Bubble size scaling applies to all figures. Numbers refer to sample IDs (see Supplementary Table 2).

Figure 6. Denudation rate vs slope. A: For humid (purple) and arid (orange) conditions along the Chilean Andes Orogen. Purple and orange lines are models[41] considering 54% and 60% for critical slopes. Error bars refer to ± 1σ. B: Denudation rate vs slope. The violet circles refer to compiled ^{10}Be denudation rates from the OCTOPUS database[35] from New Zealand[38,39] and the Pacific Northwest[40]. The blue circles refer to humid Chile[42–44] and our new data, that is highlighted by the grey frame. Circle size scales with $\log_{10}$ of catchment size, and purple dashed line is the refers to the purple model in A [41].

Figure 7. A: Denudation rates, forest cover, mean elevation, slope, mean annual precipitation (MAP), and aridity index (AI) along a N-S transect of the Chilean Main Cordillera. Red and violet squares refer to arid and humid climate, respectively. B: Scaling between denudation rates and the aridity index for humid climate, i.e., AI >1 (R^2 =0.84, 10,000 Monte-Carlo simulations, $y=-1.625\pm0.10 * 4.925\pm0.55^X$), squares scale with NDVI (Normalized Difference Vegetation Index).

Figure 8. A: Relative variable importance for humid (n=12) and arid (n=50) conditions, respectively, for the random forest regression of ^{10}Be denudation rates from Chile (see SI). All predictor variable importance was normalized to 100% (see SI), color density scales with relative importance. B: Observed vs predicted values for standardized denudation rates for humid (purple) and arid (red) conditions, respectively. Purple and red lines refer to linear regressions; grey dashed line refers to the 1:1-line. We treat latitude, however, as a metric that integrates large scale climatic and environmental conditions, thus largely mimicking AI.

SUPPLEMENTARY INFORMATION

Sampled Catchments

The topography of Northern Chilean Patagonia is largely a product of quaternary volcanism and massive glacial erosion. The latter carved deep fjords between eroded islands and peninsulas, leaving behind a spectacular landscape of steep slopes and small cirques in headwaters mounting above broad, flat-bottomed valleys[63]. All catchments drain into the Pacific Ocean (see as an example Supplementary Figure 5).

The regional tectonics are dominated by active subduction and intra-arc strike-slip motion along the Southern Chile Trench and the Liquiñe-Ofqui Fault zone[64], respectively, and Quaternary arc volcanism. Among them, the Chaitén, Michinmahuida and Corcovado volcanoes are prominent landscape features and belong to the Andean Southern Volcanic Zone (SVZ).

We collected (n = 5) new samples of fluvial sediment in headwater catchments draining parts of the Northern Chilean Patagonian Andes (43°0'-45°40'S) from north to south along a transect from Chaitén township to the cities of Coyhaique and Puerto Aysén (Figure 1). Given restricted accessibility due to dense forest, we sampled headwater catchments that are accessible from the main roads, i.e., along the Carretera Austral. All headwaters drain into the Pacific Ocean via the connecting Yelcho, Palena, of Aysén rivers. Dense coastal rainforest dominates all catchments. Our sampled catchments do not extent into highest-andine regions. Such fact minimizes effects of glacial and snow cover on shielding on cosmogenic-derived denudation rates.

Our data are the first to fill the Andean gap between 41° and 52°S. The most proximal reported denudation rates, i.e., north of 41°S and south of 52°S, are at the order of <0.2 m kyr^{-1} [Ref65,66]. Yet, we regard these rates as comparable to a limited degree only. For example, rates from ~ 52°S based on decennial sediment flux monitoring originate east from the Andean divide in the much drier

Pampean region[65]. Likewise, comparison to exhumation rates derived from low-temperature thermochronology yielding 0.2-0.7 m kyr^{-1} along the Patagonian Andes[56–58] is also limited due to different time scales constrained. Thermochronology derived rates average a period, of which we can assume at most the last 16,000 years as comparable to the current environmental, particularly forest, conditions[e.g., 20].

^{10}Be sampling and lab procedure

Secondary cosmic radiation reacts with minerals of Earth surface producing cosmogenic nuclides such as ^{10}Be, which production rates are well known for quartz[67]. The production rate of a mineral decreases exponentially at depth. When minerals reach a steadily ^{10}Be concentration, it scales inversely with the rate of surface removal[67,68]. That surface removal, here called denudation, involves both physical erosion and chemical weathering. The quartz present in well-mixed fluvial sediments provides spatially averaged erosion rates from upstream areas, which may range from single hillslopes to continental river basins[13]. The timescale for a steadily erosion rate refers to the mineral residence time within the particle mean free path in rocks[67]. That is, the characteristic time τ necessary to erode a ~60 cm thickness strip[13]

Samples were prepared for cosmogenic ^{10}Be analysis at the University of Wollongong. Quartz was purified following procedures described in[69] using froth flotation to separate feldspars from quartz, and Be was separated following procedures described in[70]. Samples were spiked with ≈250 µg of ^{9}Be from a low-level beryl carrier solution added prior to complete HF dissolution. Sample purity was assessed following dissolution in HF, with native Al concentrations in all samples being < ≈200 ppm (average = 168 ppm). To test for the presence of native ^{9}Be in our

samples, we also measured the Be concentration via ICP-OES in the dissolved material, obtaining concentration differences < 3%, the typical uncertainty of the method (average difference ≈1%).

$^{10}Be/^{9}Be$ ratios were measured using the 6MV SIRIUS facility at ANSTO[71] and were normalised to the KN-5-2, KN-5-4, and KN-6-2 Ref72 standards. Analytical uncertainties for the final ^{10}Be concentrations (atoms g^{-1}) include AMS measurement uncertainties (larger of counting statistics or standard deviation of repeats and blank corrections) in quadrature with 1-2% for ^{10}Be standard reproducibility (depending on the individual AMS measurement conditions) and 1% uncertainty in the ^{9}Be carrier concentration.

Denudation rates were calculated using the open-source program CAIRN v.1[73]. Basin-averaged nuclide production from neutrons and muons was calculated with the approximation of[74] and using a sea-level and high-latitude total production rate of 4.3 atoms g^{-1} yr^{-1} Ref73. Production rates for catchment-wide denudation rates were calculated at every grid cell of a hydrologically enforced 90 m SRTM DEM[75], using the time-independent Lal/Stone scaling scheme[76]. Atmospheric pressure was calculated via interpolation from the NCEP2 reanalysis data[77]. Topographic shielding was calculated from the same DEM using the method of[78] with $\Delta\theta = 8°$ and $\Delta\phi = 5°$.

All data that we used here as for comparison reasons were obtained from the OCTOPUS database[35] and[66]. We recalculated the data of[44,66] using the Octopus protocol. Our new data are calculated in the same way. The differences from all recalculated and original data[44,66] were minor, i.e. the ratio was 0.969±0.112 (see Supplementary Table 4).

GIS-computations

We ran all spatial computations to calculate catchment-wide covariates in QGIS 3.2.2, GRASS 7.8.2 and SAGA 2.3.2. To this end we derived topographic metrics such as elevation and local slope from SRTM digital elevation models, i.e. 30 and 90m ground resolution[75] to both broadly characterize the topography and also being consistent with the OCTOPUS data. We extracted catchment-wide mean annual precipitation from the CHIRPS v2 product evaluated for Chile by[79] the tree cover percent from[37], the bare surfaces from[80] and the aridity[34,81]. The latter can be expressed by the dimensionless Aridity Index (AI) that is defined as

$$AI = \frac{MAP(mm)}{MAE(mm)} \qquad \text{(eq. 1)}$$

where MAP refers to mean annual precipitation and MAE to mean annual potential evapotranspiration. MAE is calculated using the Hargreaves model and validated using n = 2288 Penman-Monteith values at climate stations in South America (and Africa)[81]. We estimated spectral indices such as NDVI within each catchment using Google Earth Engine[82]. Mean NDVI was computed on COPERNICUS/S2_SR collection of January 2021 with less than 20% of cloudy pixel percentage (https://developers.google.com/earth-engine/datasets/catalog/COPERNICUS_S2_SR#description).

Calculation of landslide erosion rates

We used the landslide inventories of[30] who approximated the total affected area for each landslide, that is source, runout, and deposition zones. We used the landslide area and calculated the volume of the eroded material by assigning a maximum depth of the landslide slide plane of 2m consistent with[29], who measured the geometry of landslides around Chaitén volcano from photogrammetric unmanned aerial vehicle (UAV) surveys and randomly confirmed landslide scar

and deposit depth using measuring tape and an inclinometer. At none of these sites did we find deposits thicker than about 2 m.

Next, we averaged the calculated landslide volume (L^3) across the area(s) (L^2). The total area of Huequi peninsula is 897 km^2, Chaitén (2,413 km^2), and Calbuco (4,750 km^2)[30]. Lastly, we divided calculated height (L, here as m) by the period (20 years) covered by the landslide inventory. We approximated the date of landslide occurrence at annual precision judging from the timestamps of image pairs showing the latest undisturbed conditions and the earliest landslide occurrence. We recorded 411 landslides (total landslide area: 32.7 km2) during 2001-2019 for Calbuco, 616 landslides (total landslide area: 19.4 km2) during 2001-2019, and 38 landslides for Huequi (total landslide area: 3,4 km2) during 2001-2019. The results are shown in Supplementary Table 3.

Data Analysis on denudation rates

We used Random Forest regression[83] to identify the most relevant topographic, climatic, and disturbance-related controls on the denudation rates for Chile (see Supplementary Table 1). Random forests (RF) are ensembles of decision trees trained on data, forming a robust nonparametric model capable of handling large nonlinear, noisy, fragmented, or correlated multidimensional data for classification[84,85], and combine bootstrap aggregating with random variable selection[83]. The strategy is to explore the importance of predictors using bootstrapped data and predictor subsets for growing decision trees. Our response variable refers to the erosion rates (mm/year). Predictor variables include continuous data on hydro-climatology, geology, land cover and topography. We grew random forests with 10,000 individual trees, setting the number of variables at each node to 2 (out of a total of 9 predictors, see Figure 4). We assessed relative

608 variable importance for a random forest regression of 10Be denudation rates. To this end, we
609 normalized all predictor variable importance to 100%. We employ Random Forest (RF) statistics
610 to quantify controls for the observed erosion rates. Our RF-model fit was good for humid
611 conditions, but poor for arid conditions (R^2=0.62 vs R^2=0.06).

612 We calculated the critical slope following [49] using ordinary least square modeling fitting
613 for humid (AI>1) and arid (AI<1) subsets of our data compilation for the Chilean Andes orogen.

614 Comparing to other similar landscapes, we excluded data from Hopkins and Dobson valley,
615 NZ, [39] that are locally affected by deep-seated landslides, thus comprise a different process domain.
616 We also excluded the work by[86] as these catchments are dominated by shrublands and/or extend
617 into high-alpine terrain[86] in contrast to our catchments.

618

Supplementary Table

Supplementary Table 1. Properties of studied catchments. Slope and elevation come from 90m SRTM data[75], MAP from satellite-based rainfall product CHIRPS 1981-2016 [Ref79], AI comes from[34,81] from, forest cover from[37], and fraction of granitic lithology with respect to total catchment area from[33]. Uncertainty is given as ± 1σ.

Sample ID	BE10-01	BE10-08	BE10-13	BE10-14	BE10-15
Lat (º)	-43.1676	-43.8284	-45.4609	-45.4593	-45.3626
Lon (º)	-72.4277	-72.3521	-72.3238	-72.3426	-72.5708
Slope (%)	58.2 ± 28.1	51.6 ± 25.6	70.5 ± 32.5	57.1 ± 28.4	49.9 ± 25.3
Catchment (km2)	28. 44	18.00	10.81	4.09	8.53
MAP (mm)	2528	2703	1635	1731	2513
Elevation (m asl)	921 ± 308	838 ± 473	983 ± 315	823 ± 288	866 ± 274
AIMedian	2.06	2.02	1.66	1.79	2.04
Forest cover (%)	60.8	69.5	52.5	72.3	76.7
Granitic (%)	40.2	96	100	99.1	97.9

Supplementary Table 2. Summary of cosmogenic ^{10}Be measurements and calculated denudation, uncertainty is given as ± 1σ

Sample ID	UOW Sample ID	ANSTO Cathode ID	Total Qtz (g)	^{9}Be Spike (µg)	^{27}Al ICP (µg.g^{-1})	^{9}Be ICP (µg)	%Diff ^{9}Be[a]	^{10}Be/^{9}Be[b,c] (10^{-15})	^{10}Be[c] (atoms.g^{-1})	CAIRN Total Scaling Factor	Erosion Rate[c] (mm.yr^{-1})	Averaging Timescale (kyr)
BE-10-1	UOW001	Be829	40.160	263.9	203.9	257.6	2.43	16.90 ± 0.94	7421 ± 443	2.13	0.83 ± 0.18	0.7
BE-10-8	UOW002	Be830	39.985	261.5	173.9	261.8	0.11	18.11 ± 1.00	7912 ± 471	2.14	0.79 ± 0.17	0.8
BE-10-13	UOW003	Be831	40.367	261.9	144.6	262.2	0.10	24.49 ± 1.23	10618 ± 584	2.31	0.63 ± 0.13	1.0
BE-10-14	UOW004	Be832	40.118	261.5	189.7	263.2	0.67	19.76 ± 1.13	8604 ± 527	2.03	0.69 ± 0.15	0.9
BE-10-15	UOW005	Be833	40.236	262.3	128.4	259.3	1.17	30.28 ± 1.37	13192 ± 665	2.13	0.47 ± 0.10	1.3

a) difference between ^{9}Be spike added and ^{9}Be measured in dissolved sample via ICP-OES

b) corrected using a procedural blank with ^{10}Be/^{9}Be = 0.483 ± 0.165 x 10^{-15} (n=5)

c) uncertainties at 1-sigma level

630 Supplementary Table 3. Landslide erosion rates estimated for three areas within the CTR of
631 northern Patagonia: 1) Calbuco area (affected by the Calbuco eruption in 2015; 2) Huequi area
632 (without relevant human or natural disturbances and used as representing undisturbed state); 3)
633 Chaitén area where rainforest stand in various states of post-volcanic disturbance following the
634 2008 Chaiten eruption.
635

Study area	Reference coordinates		Total volume (km3)	Landslide erosion (m kyr^{-1})
	Lat (º)	Long (º)		
Calbuco	-41.1917	-72.4909	0.06542	0. 72
Huequi	-42.3680	-72.5919	0.00678	0. 39
Chaiten	-42.7799	-72.5222	0.03882	0. 84

636
637

638

639 Supplementary Table 4. New and compiled [66] data of detrital ^{10}Be concentration and denudation rates for samples of grain size

640 between 0.126-1 mm within Chilean Western Andes. *Denudation rates recalculated for Octopus database in this work.

Name and reference	Cosmogenic Nuclide Concentration (at/g) Carretier et al. 2018	Cosmogenic Nuclide Concentration uncertainty (at/g) Carretier et al 2018	Cosmogenic Nuclide Concentration (at/g) Octopus	Cosmogenic Nuclide Concentration uncertainty (at/g) Octopus	Denudation rate (mm/a) Carretier et al 2018	Denudation rate uncertainty (mm/a) Carretier et al 2018	Denudation rate (mm/a) Octopus	Denudation rate uncertainty (mm/a) Octopus
BE10-01			7421*	443*			0.831*	0.177*
BE10-08			7912*	471*			0.786*	0.167*
BE10-13			10618*	584*			0.626*	0.131*
BE10-14			8604*	527*			0.687*	0.147*
BE10-15			13192*	665*			0.469*	0.098*
MAU1[50]	129351	14825	129351	7413	0.090	0.017	0.102	0.020
LON1[50]	64381	29145	64381	14573	0.121	0.058	0.175	0.053
TEN1[50]	73331	48099	73331	24050	0.170	0.114	0.163	0.067
TIN1[50]	99370	5275	99370	2638	0.159	0.025	0.163	0.030
CAC1[50]	91404	10713	91404	5357	0.195	0.037	0.194	0.037
MAI1[50]	87032	5010	87032	2505	0.250	0.040	0.257	0.047
ACO1[50]	101191	2915	101191	1458	0.194	0.030	0.211	0.038
CHO1[50]	195648	6708	195648	3354	0.059	0.009	0.067	0.012
CHO0820[50]	234948	10795	234948	5398	0.040	0.006	0.047	0.009
CHO0822S[50]	198207	5803	198207	2902	0.053	0.008	0.061	0.012
CHO0823S[50]	218067	9450	218067	4725	0.048	0.008	0.055	0.010
ILL1[50]	468966	13507	468966	6754	0.030	0.005	0.031	0.006
HUR1[50]	593076	38635	593076	19318	0.043	0.007	0.036	0.007
ELK1[50]	177039	23322	177039	11661	0.129	0.026	0.149	0.029
ELK2[50]	186943	16714	186943	8357	0.122	0.021	0.141	0.026
HUA1[50]	479983	13641	479983	6821	0.050	0.008	0.052	0.009
HUA7[50]	833051	53481	833100	53500	0.029	0.005	0.028	0.005
HUA10[50]	588998	16567	589000	16600	0.039	0.006	0.038	0.007
HUA12[50]	598649	24962	598600	25000	0.037	0.006	0.035	0.007
SAN1[50]	1027511	153842	1027511	76921	0.019	0.004	0.017	0.003
CHIZ1[87]	116710	17124	117000	17000	0.062	0.013	0.077	0.019

LL1[88]	1069000	56000	1069000	56000	0.024	0.004	0.023	0.004
LL2[88]	975000	40000	975000	40000	0.023	0.004	0.023	0.004
LL3[88]	866000	54000	866000	54000	0.025	0.004	0.0238	0.00463
LL4[88]	2435000	3000000	2435000	306000	0.012	0.014	0.011	0.002
LL5[88]	2373000	1490000	2373000	149000	0.012	0.008	0.011	0.002
Bbd2-2[44,66]	75957	9631	75957*	9631*	0.063	0.012	0.075*	0.018*
Bbm1-2[42]	116638	9459	117000	9460	0.061	0.010	0.066	0.014
D1-1[42]	86277	14037	86300	14000	0.074	0.016	0.064	0.017
C1-1b[44,66]	113680	20735	113680*	20735*	0.041	0.010	0.039*	0.011*
C3-2[44,66]	97896	8272	97896*	8272*	0.039	0.007	0.037*	0.009*
VC1-2[44,66]	95900	10529	95900*	10529*	0.042	0.008	0.042*	0.011*
LC1[44,66]	89686	24690	89686*	24690*	0.062	0.019	0.073*	0.026*
Ca1[44,66]	35951	2506	35951*	2506*	0.162	0.027	0.154*	0.034*
R1[44,66]	252782	8226	252782*	8226*	0.014	0.002	0.013*	0.003*
H1[44,66]	41242	3172	41242*	3172*	0.159	0.027	0.148*	0.032*
Mi2[44,66]	93772	4280	93772*	4280*	0.037	0.006	0.035*	0.008*

641

642

643 **Supplementary Figure**

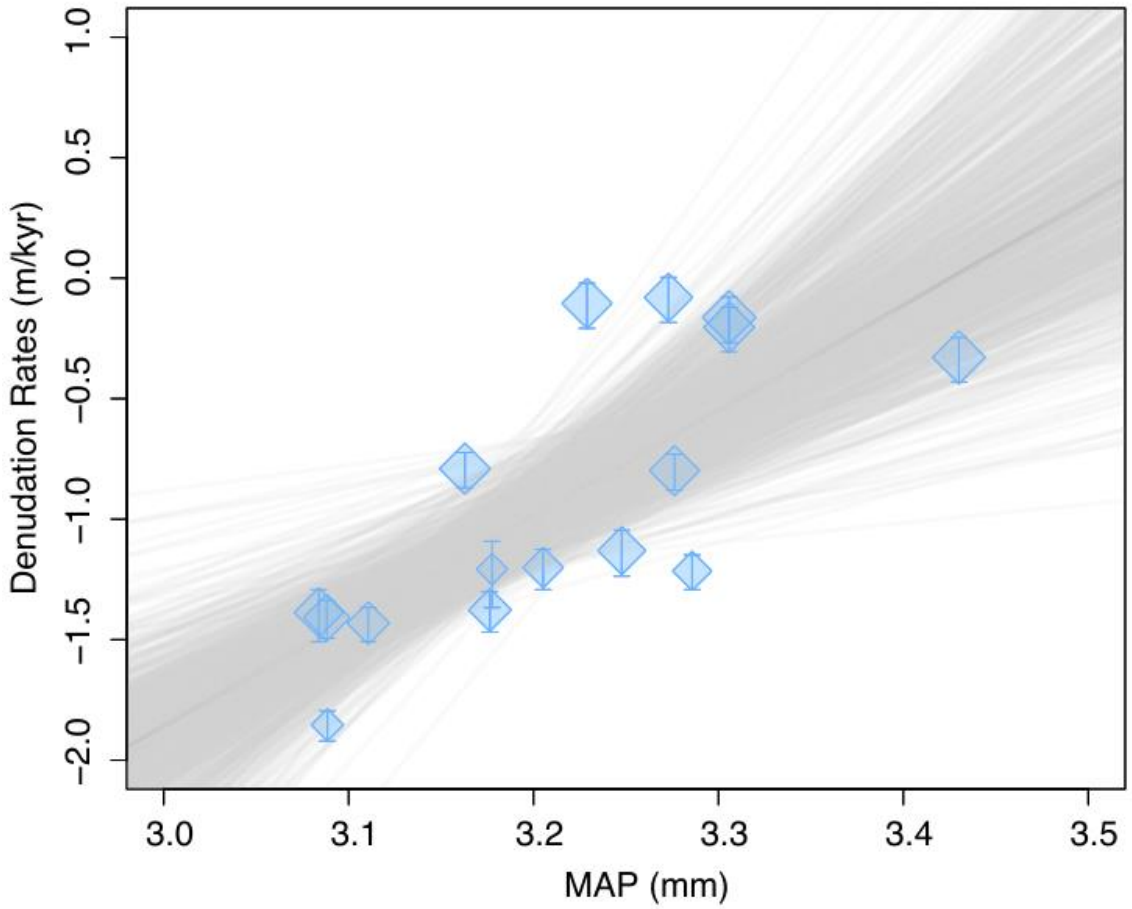

644

645 Supplementary Figure 1. Denudation rate vs MAP, log-scaled, 10,000 MC simulations, Y = -14.951 ± 3.40

646 * 4.364 ± 1.059^{X}; R^2=0.517. Square size scales with $\log_{10}$ of NDVI.

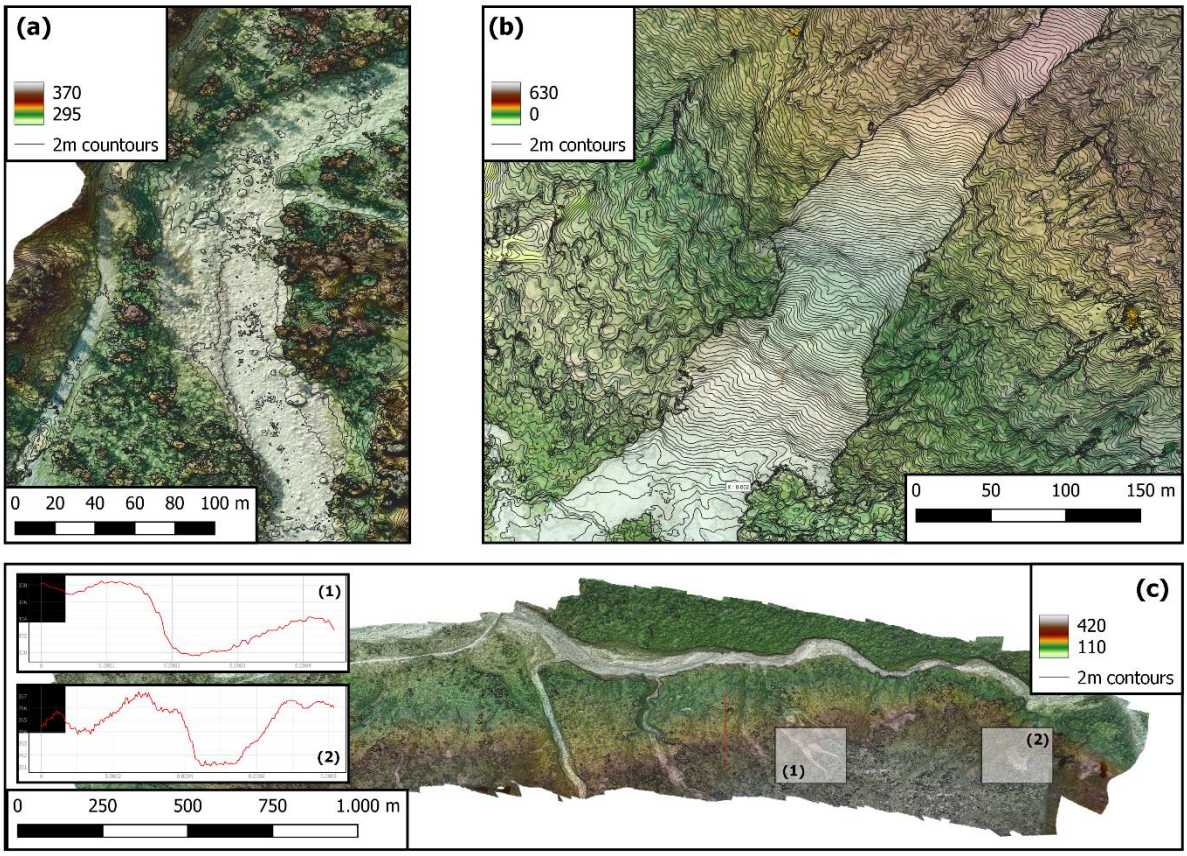

Supplementary Figure 2. RGB UAV-footage. (a) of active channel of Turbio river, boulder of up to 6 m edge lengths (42°57'16.16"S, 72°23'39.51"W), (b) rare deep landslide close to Chaitén township (42°57'1.00"S, 72°38'37.88"W), (c) shallow landsliding on the northern hillslopes of Chaitén volcano (42°48'24.48"S, 72°37'30.61"W). All UAV footage was obtained in 2018 using a Sensefly eBee RTK (a,c) and DJI Mavic Pro (b). Numbers in (c) refer to contour-parallel profiles through recent landslides.

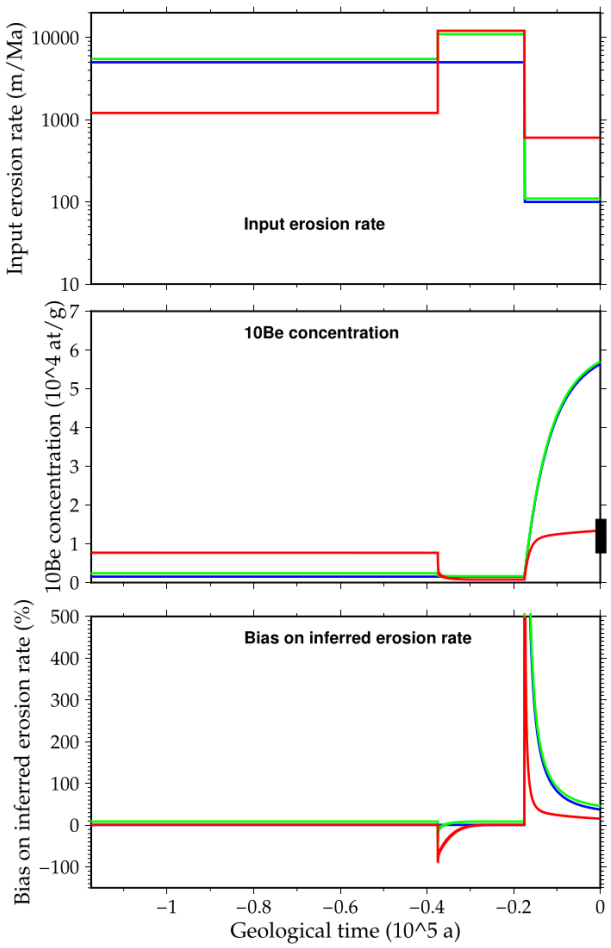

Supplementary Figure 3. Test of a possible glacial erosion inheritance. We test if our denudation rates could be biased by higher erosion during last glacial maximum and thus be less than estimated, for example 0.1 m/kyr rather than 0.5 mm/a. We test 3 scenarios with 2 pre-17.5 ka periods with higher erosion rates over 80 ka. Whatever these rates, the bias on the estimated erosion rate using riverine ^{10}Be is low. For the red scenario, that predicts the correct ^{10}Be concentration (see black rectangle in the middle panel), the bias is < 10 % even if the last glacial maximum corresponded to erosion rates as high as 10 m/kyr. The ^{10}Be production rate is 10 at/g/yr in each case and the ^{10}Be concentration is calculated using muon and neutron productions [89] as well as radioactive decay.

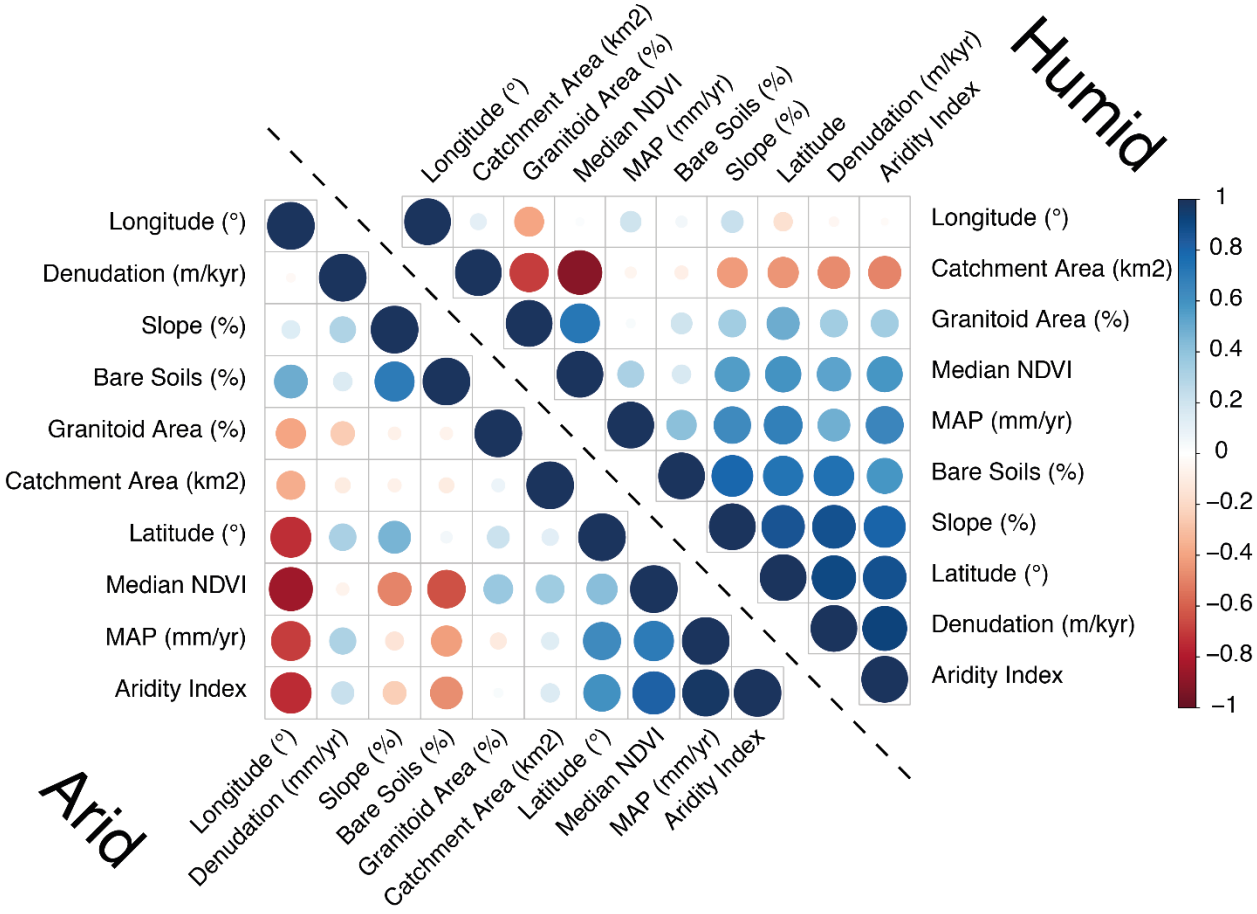

Supplementary Figure 4. Correlation plot illustrating multicollinearities between denudation and hydroclimatic, geological, and spatial predictors grouped for arid (AI<1) and humid (AI>1) areas in Chile[42–44]. New data is included.

Supplementary Figure 5. 360° panorama view of Caleta Gonzalo catchment (42°34’06.91’’S, 72°37’42.60’’). highlighting dense Patagonian coastal temperate rainforest closely connected to the Pacific Ocean. Drone footage was acquired using a DJI Phantom 4 by Benjamin Sotomayor in 03/2022.

Supplementary References

1. Bonan, G. B. Forests and Climate Change: Forcings, Feedbacks, and the Climate Benefits of Forests. *Science (1979)* **320**, 1444–1449 (2008).
2. Canadell, J. G. & Raupach, M. R. Managing forests for climate change mitigation. *Science (1979)* **320**, 1456–1457 (2008).
3. Sidle, R. C. & Ochiai, H. Land Use and Global Change. in *Landslides: Processes, Prediction, and Land Use* 1–76 (2006).
4. Korup, O., McSaveney, M. J. & Davies, T. R. H. Sediment generation and delivery from large historic landslides in the Southern Alps, New Zealand. *Geomorphology* **61**, 189–207 (2004).
5. Hilton, R. G., Meunier, P., Hovius, N., Bellingham, P. J. & Galy, A. Landslide impact on organic carbon cycling in a temperate montane forest. *Earth Surface Processes and Landforms* **36**, 1670–1679 (2011).
6. Mohr, C. H., Korup, O., Ulloa, H. & Iroumé, A. Pyroclastic Eruption Boosts Organic Carbon Fluxes Into Patagonian Fjords. *Global Biogeochemical Cycles* **31**, 1626–1638 (2017).
7. Starke, J., Ehlers, T. A. & Schaller, M. Latitudinal effect of vegetation on erosion rates identified along western South America. *Science (1979)* **367**, 1358–1361 (2020).
8. Langbein, W. B. & Schumm, S. A. Yield of sediment in relation to mean annual precipitation. *Transactions, American Geophysical Union* **39**, 1076 (1958).
9. Acosta, V. T. *et al.* Effect of vegetation cover on millennial-scale landscape denudation rates in East Africa. *Lithosphere* **7**, 408–420 (2015).
10. Schmid, M., Ehlers, T. A., Werner, C., Hickler, T. & Fuentes-Espoz, J. P. Effect of changing vegetation and precipitation on denudation - Part 2: Predicted landscape response to transient climate and vegetation cover over millennial to million-year timescales. *Earth Surface Dynamics* **6**, 859–881 (2018).
11. Vanacker, V. *et al.* Restoring dense vegetation can slow mountain erosion to near natural benchmark levels. *Geology* **35**, 303 (2007).
12. Turner, M. G., Romme, W. H., Gardner, R. H., O’neill, R. v & Kratz, T. K. *A revised concept of landscape equilibrium: Disturbance and stability on scaled landscapes*. *Landscape Ecology* vol. 8 (1993).
13. Granger, D. E. & Schaller, M. Cosmogenic Nuclides and Erosion at the Watershed Scale. *Elements* **10**, 369–373 (2014).
14. Schaefer, J. M. *et al.* Cosmogenic nuclide techniques. *Nature Reviews Methods Primers* **2**, 18 (2022).
15. Myers, N., Mittermeier, R. A., Mittermeier, C. G., da Fonseca, G. A. B. & Kent, J. Biodiversity hotspots for conservation priorities. *Nature* **403**, 853–858 (2000).

16. Keith, H., Mackey, B. G. & Lindenmayer, D. B. Re-evaluation of forest biomass carbon stocks and lessons from the world's most carbon-dense forests. *Proc Natl Acad Sci U S A* **106**, 11635–11640 (2009).
17. DellaSala, D. A. *Temperate and Boreal Rainforests of the World: Ecology and Conservation*. (Island Press/Center for Resource Economics, 2011). doi:10.5822/978-1-61091-008-8.
18. Alaback, P. Comparative ecology of temperate rainforests of the Americas along analogous climatic gradients. *Revista Chilena de Historia Natural* **64**, 399–412 (1991).
19. de La Barrera, F., Reyes-Paecke, S. & Meza, L. Landscape analysis for rapid ecological assessment of relocation alternatives for a devastated city. *Revista Chilena de Historia Natural* **84**, 181–194 (2011).
20. Moreno, P. I. *et al.* Radiocarbon chronology of the last glacial maximum and its termination in northwestern Patagonia. *Quaternary Science Reviews* **122**, 233–249 (2015).
21. de Porras, M. E. *et al.* Postglacial vegetation, fire and climate dynamics at Central Chilean Patagonia (Lake Shaman, 44°S). *Quaternary Science Reviews* **50**, 71–85 (2012).
22. Torrejón, F., Cisternas, M., Alvial, I. & Torres, L. Colonial timber felling consequences of the alerce forests in Chiloé, southern Chile (18th and 19th centuries). *Magallania (Punta Arenas)* **39**, 75–95 (2011).
23. Urbina, M. X. Análisis histórico-cultural del alerce en la Patagonia septentrional occidental, Chiloé, siglos XVI al XIX. *Magallania (Punta Arenas)* **39**, 57–73 (2011).
24. Buma, B. *et al.* Emergent freeze and fire disturbance dynamics in temperate rainforests. *Austral Ecology* **44**, 812–826 (2019).
25. Markgraf, V. & Huber, U. M. Late and postglacial vegetation and fire history in Southern Patagonia and Tierra del Fuego. *Palaeogeography, Palaeoclimatology, Palaeoecology* **297**, 351–366 (2010).
26. Sommerfeld, A. *et al.* Patterns and drivers of recent disturbances across the temperate forest biome. *Nature Communications* **9**, (2018).
27. Morales, B. *et al.* A comparative machine learning approach to identify landslide triggering factors in northern Chilean Patagonia. *Landslides* **18**, 2767–2784 (2021).
28. Sepúlveda, S. A., Serey, A., Lara, M., Pavez, A. & Rebolledo, S. Landslides induced by the April 2007 Aysén fjord earthquake, Chilean Patagonia. *Landslides* **7**, 483–492 (2010).
29. Korup, O., Seidemann, J. & Mohr, C. H. Increased landslide activity on forested hillslopes following two recent volcanic eruptions in Chile. *Nature Geoscience* 2–8 (2019) doi:10.1038/s41561-019-0315-9.
30. Parra, E., Mohr, C. & Korup, O. Predicting Patagonian Landslides: Roles of Forest Cover and Wind Speed. (2021) doi:10.1029/2021GL095224.
31. Mohr, C. H., Manga, M., Wang, C. Y. & Korup, O. Regional changes in streamflow after a megathrust earthquake. *Earth and Planetary Science Letters* **458**, 418–428 (2017).
32. Veblen, T. Forest development in tree-fall gaps in the temperate rain forest of Chile. *Natl. Geogr. Res.* **1**, 162–183 (1985).
33. Sernageomin. Mapa geologico de chile: version digital. *Publicacion Geologia Digital* vol. 4 25 (2003).
34. Zomer, R. J. *et al. Trees and Water: Smallholder Agroforestry on Irrigated Lands in Northern India*. *IWMI report* (2007).
35. Codilean, A. T. *et al.* OCTOPUS: an open cosmogenic isotope and luminescence database. *Earth System Science Data* **10**, 2123–2139 (2018).

36. Müller Schmied, H. *et al.* Sensitivity of simulated global-scale freshwater fluxes and storages to input data, hydrological model structure, human water use and calibration. *Hydrology and Earth System Sciences* **18**, 3511–3538 (2014).
37. Hansen, M. C. *et al.* High-Resolution Global Maps of 21st-Century Forest Cover Change. *Science (1979)* **342**, 850–853 (2013).
38. Burdis, A. J. Denudation rates derived from spatially-averaged cosmogenic nuclide analysis in Nelson/Tasman catchments, South Island, New Zealand. (Victoria University of Wellington, 2014).
39. Bellingham, M. F. Climatic effects on rapid chemical and physical denudation rates measured with cosmogenic nuclides in the Ōhau catchment, New Zealand. (Victoria University of Wellington, 2020).
40. Moon, S. *et al.* Climatic control of denudation in the deglaciated landscape of the Washington Cascades. *Nature Geoscience* **4**, 469–473 (2011).
41. Roering, J. J., Perron, J. T. & Kirchner, J. W. Functional relationships between denudation and hillslope form and relief. *Earth and Planetary Science Letters* **264**, 245–258 (2007).
42. Carretier, S. *et al.* Erosion in the Chilean Andes between 27°S and 39°S: tectonic, climatic and geomorphic control. *Geological Society, London, Special Publications* **399**, 401–418 (2015).
43. Carretier, S. *et al.* Differences in 10Be concentrations between river sand, gravel and pebbles along the western side of the central Andes. *Quaternary Geochronology* **27**, 33–51 (2015).
44. Tolorza, V. Magnitude and Dynamics of catchment erosion in the Biobío River Basin. (Universidad de Chile, 2015).
45. Mishra, A. K., Placzek, C. & Jones, R. Coupled influence of precipitation and vegetation on millennial-scale erosion rates derived from 10Be. *PLOS ONE* **14**, e0211325 (2019).
46. Alvarez-Garreton, C. *et al.* The CAMELS-CL dataset: catchment attributes and meteorology for large sample studies – Chile dataset. *Hydrology and Earth System Sciences Discussions* 1–40 (2018) doi:10.5194/hess-2018-23.
47. Urrutia-Jalabert, R., Malhi, Y. & Lara, A. The Oldest, Slowest Rainforests in the World? Massive Biomass and Slow Carbon Dynamics of Fitzroya cupressoides Temperate Forests in Southern Chile. *PLOS ONE* **10**, e0137569 (2015).
48. Mohr, C. H., Manga, M., Wang, C., Kirchner, J. W. & Bronstert, A. Shaking water out of soil. *Geology* **43**, 207–210 (2015).
49. Hales, T. C. & Roering, J. J. Climatic controls on frost cracking and implications for the evolution of bedrock landscapes. *Journal of Geophysical Research* **112**, F02033 (2007).
50. Carretier, S. *et al.* Slope and climate variability control of erosion in the Andes of central Chile. *Geology* **41**, 195–198 (2013).
51. Sidle, R. C. A Conceptual Model of Changes in Root Cohesion in Response to Vegetation Management. *Journal of Environmental Quality* **20**, 43–52 (1991).
52. Vorpahl, P., Dislich, C., Elsenbeer, H., Märker, M. & Schröder, B. Biotic controls on shallow translational landslides. *Earth Surface Processes and Landforms* **38**, 198–212 (2013).
53. Spors, S. Suicidal forests ? – Modelling biomass surcharge as a potential landslide driver in temperate rainforests of Chilean Patagonia. (Universität Potsdam, 2021).
54. Larsen, I. J., Montgomery, D. R. & Korup, O. Landslide erosion controlled by hillslope material. *Nature Geoscience* **3**, 247–251 (2010).

55. Amundson, R., Heimsath, A., Owen, J., Yoo, K. & Dietrich, W. E. Hillslope soils and vegetation. *Geomorphology* **234**, 122–132 (2015).
56. Fosdick, J. C., Grove, M., Hourigan, J. K. & Calderón, M. Retroarc deformation and exhumation near the end of the Andes, southern Patagonia. *Earth and Planetary Science Letters* **361**, 504–517 (2013).
57. Andrić-Tomašević, N. *et al.* Quantifying Tectonic and Glacial Controls on Topography in the Patagonian Andes (46.5°S) From Integrated Thermochronometry and Thermo-Kinematic Modeling. *Journal of Geophysical Research: Earth Surface* **126**, (2021).
58. Georgieva, V. *et al.* Tectonic control on rock uplift, exhumation, and topography above an oceanic ridge collision: Southern Patagonian Andes (47°S), Chile. *Tectonics* **35**, 1317–1341 (2016).
59. Gray, A. N., Whittier, T. R. & Harmon, M. E. Carbon stocks and accumulation rates in Pacific Northwest forests: Role of stand age, plant community, and productivity. *Ecosphere* **7**, 1–19 (2016).
60. Stephenson, N. L. *et al.* Rate of tree carbon accumulation increases continuously with tree size. *Nature* **507**, 90–93 (2014).
61. Frith, N. v. *et al.* Carbon export from mountain forests enhanced by earthquake-triggered landslides over millennia. *Nature Geoscience* **11**, 772–776 (2018).
62. Smith, R. W., Bianchi, T. S., Allison, M., Savage, C. & Galy, V. High rates of organic carbon burial in fjord sediments globally. *Nature Geoscience* **8**, 450–453 (2015).
63. Singer, B. S., Ackert, R. P. & Guillou, H. 40Ar/39Ar and K-Ar chronology of Pleistocene glaciations in Patagonia. *Geological Society of America Bulletin* **116**, 434 (2004).
64. Cembrano, J., Hervé, F. & Lavenu, A. The Liquiñe Ofqui fault zone: a long-lived intra-arc fault system in southern Chile. *Tectonophysics* **259**, 55–66 (1996).
65. Pepin, E., Carretier, S., Guyot, J. L. & Escobar, F. Specific suspended sediment yields of the Andean rivers of Chile and their relationship to climate, slope and vegetation. *Hydrological Sciences Journal* **55**, 1190–1205 (2010).
66. Carretier, S. *et al.* Review of erosion dynamics along the major N-S climatic gradient in Chile and perspectives. *Geomorphology* **300**, 45–68 (2018).
67. Lal, D. Cosmic ray labeling of erosion surfaces: in situ nuclide production rates and erosion models. *Earth and Planetary Science Letters* **104**, 424–439 (1991).
68. von Blanckenburg, F. & Willenbring, J. K. Cosmogenic Nuclides: Dates and Rates of Earth-Surface Change. *Elements* **10**, 341–346 (2014).
69. Kohl, C. P. & Nishiizumi, K. Chemical isolation of quartz for measurement of in-situ -produced cosmogenic nuclides. *Geochimica et Cosmochimica Acta* **56**, 3583–3587 (1992).
70. von Blanckenburg, F., Belshaw, N. S. & O'Nions, R. K. Separation of 9Be and cosmogenic 10Be from environmental materials and SIMS isotope dilution analysis. *Chemical Geology* **129**, 93–99 (1996).
71. Wilcken, K. M. *et al.* SIRIUS Performance: 10Be, 26Al and 36Cl measurements at ANSTO. *Nuclear Instruments and Methods in Physics Research Section B: Beam Interactions with Materials and Atoms* **455**, 300–304 (2019).
72. Nishiizumi, K. *et al.* Absolute calibration of 10Be AMS standards. *Nuclear Instruments and Methods in Physics Research, Section B: Beam Interactions with Materials and Atoms* **258**, 403–413 (2007).

73. Mudd, S. M., Harel, M.-A., Hurst, M. D., Grieve, S. W. D. & Marrero, S. M. The CAIRN method: automated, reproducible calculation of catchment-averaged denudation rates from cosmogenic nuclide concentrations. *Earth Surface Dynamics* **4**, 655–674 (2016).
74. Braucher, R., Merchel, S., Borgomano, J. & Bourlès, D. L. Production of cosmogenic radionuclides at great depth: A multi element approach. *Earth and Planetary Science Letters* **309**, 1–9 (2011).
75. Jarvis, A., Reuter, H. I., Nelson, A. & Guevara, E. Hole-filled SRTM for the globe Version 4. *available from the CGIAR-CSI SRTM 90m Database* vol. 15 http://srtm.csi.cgiar.org (2008).
76. Stone, J. O. Air pressure and cosmogenic isotope production. *Journal of Geophysical Research: Solid Earth* **105**, 23753–23759 (2000).
77. Compo, G. P. *et al.* The Twentieth Century Reanalysis Project. *Quarterly Journal of the Royal Meteorological Society* vol. 137 1–28 (2011).
78. Codilean, A. T. Calculation of the cosmogenic nuclide production topographic shielding scaling factor for large areas using DEMs. *Earth Surface Processes and Landforms* **31**, 785–794 (2006).
79. Zambrano-Bigiarini, M., Nauditt, A., Birkel, C., Verbist, K. & Ribbe, L. Temporal and spatial evaluation of satellite-based rainfall estimates across the complex topographical and climatic gradients of Chile. *Hydrology and Earth System Sciences* **21**, 1295–1320 (2017).
80. Zhao, Y. *et al.* Detailed dynamic land cover mapping of Chile: Accuracy improvement by integrating multi-temporal data. *Remote Sensing of Environment* **183**, 170–185 (2016).
81. Zomer, R. J., Trabucco, A., Bossio, D. A. & Verchot, L. v. Climate change mitigation: A spatial analysis of global land suitability for clean development mechanism afforestation and reforestation. *Agriculture, Ecosystems and Environment* **126**, 67–80 (2008).
82. Gorelick, N. *et al.* Google Earth Engine: Planetary-scale geospatial analysis for everyone. *Remote Sensing of Environment* **202**, 18–27 (2017).
83. Breiman, L. Random Forests. *Machine Learning* **45**, 5–32 (2001).
84. Liaw, A. & Wiener, M. Classification and Regression by randomForest. *R News* **2**, 18–22 (2002).
85. Strobl, C., Boulesteix, A. L., Kneib, T., Augustin, T. & Zeileis, A. Conditional variable importance for random forests. *BMC Bioinformatics* **9**, 1–11 (2008).
86. Larsen, I. J. *et al.* Rapid soil production and weathering in the Southern Alps, New Zealand. *Science* **343**, 637–40 (2014).
87. Carretier, S. *et al.* A note on 10 Be-derived mean erosion rates in catchments with heterogeneous lithology: examples from the western Central Andes. *Earth Surface Processes and Landforms* **40**, 1719–1729 (2015).
88. Kober, F. *et al.* Complex multiple cosmogenic nuclide concentration and histories in the arid Rio Lluta catchment, northern Chile. *Earth Surface Processes and Landforms* **34**, 398–412 (2009).
89. Braucher, R. *et al.* Determination of muon attenuation lengths in depth profiles from in situ produced cosmogenic nuclides. *Nuclear Instruments and Methods in Physics Research Section B: Beam Interactions with Materials and Atoms* **294**, 484–490 (2013).